Coalescence characteristics of bulk nanobubbles in water: A molecular dynamics study coupled with theoretical analysis

Eric Bird ⬤, Eric Smith ⬤, and Zhi Liang ⬤*

Department of Mechanical Engineering, California State University, Fresno, California 93740, USA

The coalescence of two nanobubbles (NBs) in water is a process of great importance to many industrial applications. In this work, we study the coalescence of two equal-sized nitrogen NBs in water using molecular dynamics (MD) simulations and continuum-based theoretical analysis. We vary the NB diameter from 30 to 50 nm and study the coalescence characteristics including the expansion speed of the capillary bridge between two coalescing NBs, the dynamic regime of NB coalescence, the diameter of fully merged NBs, and the temperature variation of NBs during the coalescence process. For all cases, we show the MD simulation results can be well understood by the theoretical models developed in this work. Due to the large Laplace pressure in the model NBs, the diameter ratio of fully merged NBs to their daughter NBs is $\sqrt{2}$, which explains the recent experimental result showing that the size of NBs in water is distributed discretely with a uniform increment factor of $\sqrt{2}$ [Ma *et al.*, J. Phys. Chem. B **124**, 5067 (2020)]. The expansion of gas inside the coalescing NBs and the heat transfer between the gas NB and surrounding liquid leads to fluctuations of gas temperature during coalescence. From the theoretical analysis, we find the coalescence dynamics of NBs is in the crossover regime where neither viscous stress nor inertial stress in the surrounding liquid dominates even when the viscous stress is more than ten times higher than inertial stress. In the range of Ohnesorge number from 0.33 to 0.82, we show the scaling exponent for the capillary bridge radius vs time at late times of NB coalescence is around 0.75 ± 0.05, which is considerably higher than 0.5 in the viscous-dominated regime.

I. INTRODUCTION

Nanobubbles (NBs) are gas-filled cavities in liquids with diameters smaller than 1 μm. When the bubble size is less than 1 μm, the buoyancy effect on bubbles is insignificant compared to Brownian motion. As a result, NBs are remarkably stable compared to macrobubbles, and have been observed to remain suspended in liquids for as long as several days [1]. Due to their unique properties, NBs are extremely useful in a broad range of applications, such as froth flotation of fine or ultrafine mineral particles [2–6], wastewater treatment [7–10], detergent-free cleaning of clothes [11], and deinking of recycled paper [12]. The coalescence of two NBs is a process of great importance to many of these applications [13]. Therefore, a fundamental understanding of coalescence characteristics of NBs is required for efficient use of NBs in various industrial applications.

Despite the importance of NB coalescence in many applications, the characteristics of NB coalescence processes are not fully understood. This is mainly due to lack of experimental tools that can image the nanosecond-timescale coalescence dynamics of NBs with nanoscale spatial resolution. As a result, most experimental studies on characteristics of bubble coalescence focus

*zliang@csufresno.edu

on the coalescence dynamics of millibubbles and microbubbles [14–18]. It is not clear if the coalescence characteristics of NBs are similar to those of millibubbles and microbubbles. Recently, Ma *et al.* generated monodispersed bulk NBs in water by pushing gas through a porous alumina membrane with almost uniform pore diameters [19]. Using nanoparticle tracking analysis, Ma *et al.* measured the size distribution of NBs hours and days after gas injection and found the size of bulk NBs is distributed discretely with a uniform increment factor of $\sqrt{2}$ [19]. This result implies that the diameter ratio of a fully merged NB to that of the original NB is $\sqrt{2}$, which is different from the $\sqrt[3]{2}$ ratio that is often found in the coalescence of microbubbles or millibubbles [14]. Our recent molecular dynamics (MD) simulations in a monatomic fluid system also verifies the size ratio of $\sqrt{2}$ for the coalescence of NBs [13]. This is an example showing that the coalescence characteristics of millibubbles (or microbubbles) cannot be simply applied to NBs. Therefore, it is imperative to carry out a study on coalescence of NBs to find the differences in the coalescence characteristics between NBs and millibubbles (or microbubbles).

In this work, we resort to MD simulations coupled with theoretical analysis to study the coalescence characteristics of bulk nitrogen (N_2) NBs in water. One of the challenges in the MD simulation of NB coalescence is its high computational cost. Our recent MD simulations on the coalescence of NBs in a monatomic Lennard-Jones (LJ) fluid system show that we need over 10 000 000 atoms to model coalescence of NBs with a diameter of tens of nanometers [13]. The model system in this work contains water molecules which are polyatomic polar molecules. Allowing for a more complex potential model in the nitrogen-water system and a smaller time step size required in the MD simulation of water, the computational cost for the nitrogen-water system could be two orders of magnitude larger than that in a similarly sized monatomic LJ fluid system. Such computational cost was prohibitive in the past. Thanks to the fast growth in computing power, we are now able to use supercomputers [20] to run MD simulations to study coalescence of N_2 NBs in water which is more closely connected with experimental results than the NBs in a monatomic LJ fluid system. Observing the coalescence process of N_2 NBs in water in real time via MD simulations also allows us to understand microscopic details of NB coalescence characteristics that are inaccessible by current experimental means.

Recent experimental results imply that two NBs of the same size are more likely to coalesce in water [19]. Furthermore, if two NBs are of different sizes, both NB coalescence and the Ostwald ripening [21] could occur during the NB merging process. Therefore, to obtain a clear picture of the NB coalescence process, we focus on the coalescence of two equal-sized N_2 NBs in water in this work. In MD simulations, we will vary the size of N_2 NBs in water and study the coalescence characteristics including the coalescing speed of N_2 NBs in water, the dynamic regime of NB coalescence, the size of the fully merged NB, and the temperature variations of NBs during the coalescence process. To achieve this goal, we will monitor the time evolution of the capillary bridge and the temperature variation in the coalescing NBs from MD simulations and compare the MD simulation results to the theoretical predictions derived from the Navier-Stokes (NS) equation and thermodynamics laws. Using MD simulations coupled with theoretical analysis, we will provide a quantitative and fundamental understanding of the coalescence characteristics of N_2 NBs in water.

The rest of the paper is structured as follows. In Sec. II, we introduce the theoretical models for the prediction of (1) the evolution of the capillary bridge between two coalescing NBs, (2) the ratio of the diameter of a fully coalesced NB to that of the original NB, and (3) the temperature variation during coalescence. In Sec. III, we describe the MD model used for the study of the coalescence of two equal-sized N_2 NBs in water, and the properties of the model fluid obtained from MD simulations. In Sec. IV, we present MD simulation results and compare them with predictions from theoretical models. Finally, we close with our Conclusions.

II. THEORETICAL MODELS

A. Evolution of the gas bridge between NBs at the beginning of the coalescence

Figure 1(a) shows a schematic of a capillary bridge of radius r_b between two equal-sized NBs of radius R. From the geometry shown in Fig. 1(a), the gap $\Delta z(r_b)$ between two NBs measured in the
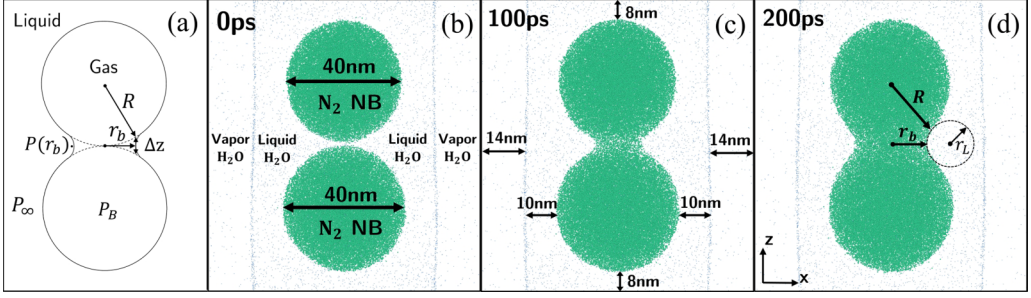
FIG. 1. (a) Schematic of coalescing NB system and (b–d) snapshots from MD simulation model. The snapshots from the MD model show 40-nm N_2 NBs coalescing in liquid water at 0, 100, and 200 ps. Green, blue, and white dots represent nitrogen, oxygen, and hydrogen atoms, respectively. The liquid water phase is hidden to clearly display the coalescing N_2 NBs and the water liquid-gas interface. In (d), r_L is the principal radius at the bridge minimum on the liquid side.

equivalent configuration before coalescence is given by

$$\Delta z(r_b) = 2R[1 - \sqrt{1 - (r_b/R)^2}]. \tag{1}$$

Since only the beginning of the coalescence process (i.e., $r_b/R < 0.45$ [18]) is considered, we use the small $(r_b/R)^2$ approximation in Eq. (1) and obtain

$$\Delta z(r_b) \approx r_b^2/R. \tag{2}$$

Substituting Eq. (2) into the continuity equation and integrating the axisymmetric Navier-Stokes (NS) equation from a quiescent point far from the bridge radius, we obtain the governing equation for r_b as a function of time t at the beginning of coalescence [13],

$$\rho\left(\frac{dr_b}{dt}\right)^2 + \rho\frac{r_b}{2}\frac{d^2r_b}{dt^2} + \frac{4\eta_L}{r_b}\frac{dr_b}{dt} = \frac{2\gamma}{R} - \frac{\gamma}{r_b} + \frac{\gamma}{r_L}, \tag{3}$$

where ρ and η_L are the density and dynamic viscosity of the liquid, respectively; γ is the surface tension at the NB liquid-gas interface; and r_L and r_b are the principal radii of curvature at the bridge minimum on the liquid side and gas side, respectively, as shown in Fig. 1. The right side of Eq. (3) is the Laplace pressure, i.e., the driving force $\Delta P = P(r_b) - P_\infty$ for the capillary bridge expansion, where $P(r_b)$ is the liquid pressure near the capillary bridge, and P_∞ is the liquid pressure at a quiescent point far from the NB interface [see Fig. 1(a)]. The derivation of Eq. (3) is shown in our previous work [13].

To solve Eq. (3) for $r_b(t)$, one needs to know the dependence of the principal radius r_L on r_b. As suggested by Thoroddsen et al. in a study of the coalescence of millibubbles [18], one can use the approximation $r_L \approx \Delta z(r_b)$ if $r_b/R < 0.45$. Hence, we set $r_L = c\Delta z(r_b)$ in the theoretical model when $r_b/R < 0.45$, where c is a dimensionless constant of order unity. Substituting the expression of r_L into Eq. (3) and rearranging the equation, we obtain the governing equation for the dimensionless bridge radius $\tilde{r}_b = r_b/R$:

$$\underbrace{\left(\tau_{\text{inert}}\frac{d\tilde{r}_b}{dt}\right)^2}_{T_i} + \underbrace{\tau_{\text{inert}}^2\frac{\tilde{r}_b}{2}\frac{d^2\tilde{r}_b}{dt^2}}_{T_a} + \underbrace{4\tau_{\text{visc}}\frac{1}{\tilde{r}_b}\frac{d\tilde{r}_b}{dt}}_{T_v} = 2 - \frac{1}{\tilde{r}_b} + \frac{0.5/c}{1 - \sqrt{1 - \tilde{r}_b^2}}, \tag{4}$$

where the characteristic inertial time is $\tau_{\text{inert}} = \sqrt{\rho R^3/\gamma}$ and the characteristic viscous time is $\tau_{\text{visc}} = \eta_L R/\gamma$. For analysis of NB coalescence dynamics, we further define the three terms from left to

right on the left-hand side of Eq. (4) as the inertial term T_i, acceleration term T_a, and viscous term T_v, respectively. We will calculate T_i, T_a, and T_v as a function of time to determine which term dominates during NB coalescence.

B. Dynamics regimes of bubble coalescence

Bubble coalescence starts with an inertially limited viscous (ILV) regime in which the dynamics is dominated by the viscous stress of gas inside the bubble. In this case, the scaling law for $r_b(t)$ is given by [17]

$$r_b/R = C_0(\gamma/\eta_g R)t,$$ (5)

where C_0 is a constant of order unity and η_g is the viscosity of gas in the bubble. In the ILV regime, $r_b \propto t$ and the capillary bridge expands very fast since η_g in Eq. (5) is usually very small. Equation (4) is not applicable in the ILV regime. Afterwards, the bubble dynamics transitions into a second regime in which Eq. (4) is applicable. In the second regime, if the coalescence dynamics is dominated by the viscous stress in the surrounding liquid [i.e., viscous term T_v in Eq. (4)], Eq. (4) gives the scaling law [13]

$$r_b/R = (1/2c)^{0.5}\sqrt{t/\tau_{\text{visc}}}.$$ (6)

Similarly, if the coalescence is dominated by the inertial stress in the surrounding liquid [i.e., inertial term T_i in Eq. (4)], Eq. (4) gives the scaling law [13]

$$r_b/R = (4/c)^{0.25}\sqrt{t/\tau_{\text{inert}}}.$$ (7)

Equations (6) and (7) are consistent with existing drop and bubble coalescence theory [17,18] in that $r_b \propto t^{0.5}$ for both the viscous-dominated regime and the inertial-dominated regime with only a difference in their characteristic timescales.

A recent experimental study on millibubble coalescence found a crossover from inertial- to viscous-dominated regimes occurs when the Ohnesorge number (Oh $= \eta_L/\sqrt{\rho\gamma R}$) is approximately 0.3 [17]. In our previous work [13], we studied the coalescence dynamics of monatomic LJ NBs with Oh in the range between 0.33 and 0.46 and found neither the inertial nor viscous terms in Eq. (4) were dominant in that range, which indicates the crossover with Oh found in the millibubble study also applies to NBs. With the nitrogen-water system in this work, we expect to have larger Oh numbers. We will investigate if we can observe a viscous-dominated regime during NB coalescence in water.

C. Size of fully merged NB

As r_b approaches and exceeds R during the coalescence, Eq. (4), which is obtained under the assumption of small $(r_b/R)^2$, becomes less accurate or even invalid. Instead of using Eq. (4), therefore, we use the Laplace pressure and the ideal gas equation to predict the size of the equilibrium NB after the two NBs fully merge.

The pressure of gas within a spherical NB of radius R in water is given by

$$P_B = P_\infty + \frac{2\gamma}{R}.$$ (8)

If the gas inside the NB is considered as an ideal gas, we have

$$P_B = \frac{Nk_BT}{\frac{4}{3}\pi R^3},$$ (9)

where N and T are the number of gas molecules and the temperature of gas in the NB, respectively, and k_B is the Boltzmann constant. If we assume the pressure of liquid water is maintained at $P_\infty = 1$ atm during bubble coalescence, we can readily predict the radius of a fully merged bubble using Eqs. (8) and (9).

If the bubble radius R is greater than a few tens of micrometers, the Laplace pressure $(2\gamma/R)$ in Eq. (8) is negligible compared to $P_\infty = 1$ atm for bubbles in water. In this case, P_B is almost a constant independent of R. Using this result in Eq. (9), we obtain $R \propto \sqrt[3]{N}$ at the same temperature. Assuming no gas molecules diffuse across the bubble surface during the coalescence process, the number of gas molecules in the fully merged bubble will be twice that in the original smaller bubble. Accordingly, the diameter ratio of a fully merged bubble to that of the original bubble is $\sqrt[3]{2}$. The $\sqrt[3]{2}$ diameter ratio was observed experimentally in the study of coalescence dynamics of microbubbles [14]. In this case, the $\sqrt[3]{2}$ diameter ratio also indicates that the volume of a fully merged bubble is equal to the total volume of two original bubbles.

For NBs in water, however, $2\gamma/R \gg P_\infty$. In this case, we have $P_B \approx 2\gamma/R$. Using this result in Eq. (9), we obtain $R \propto \sqrt{N}$. Accordingly, the diameter ratio of a fully merged NB to that of the original NB is $\sqrt{2}$. The recent experimental study shows the size of bulk NBs in water is distributed discretely with a uniform increment factor of $\sqrt{2}$ [19], which implies the $\sqrt{2}$ diameter ratio for NB coalescence in water. We will carry out MD simulations to directly measure the size of N_2 NBs in water before and after coalescence to verify the theoretical prediction.

D. Temperature variation during NB coalescence

As two NBs coalesce, the total gas volume and surface area of the NB both change with time. The expansion of the gas in coalescing NBs tends to decrease the gas temperature. Meanwhile, the heat transfer across the liquid-gas interface of the coalescing NBs tends to equilibrate the gas with the surrounding liquid water. Accordingly, we expect to observe a temperature and pressure change during coalescence. The pressure of gas inside the coalescing NBs can be readily determined using the ideal gas equation, i.e., Eq. (9), if the temperature and volume of the gas are known. Neglecting mass transfer across the NB interface, the temperature change in the coalescing NBs can be calculated using the first law of thermodynamics:

$$\delta Q - PdV = Nc_V dT, \tag{10}$$

where Q is the heat transfer across the NB interface, P and V are the pressure and volume of the gas within coalescing NBs, N is the number of gas molecules within the NB, c_V is the specific heat per molecule of gas molecules, and T is the gas temperature. For N_2 molecules at a temperature around 300 K, $c_V = 2.5k_B$ will be used in the theoretical calculation. In Eq. (10), the amount of heat transfer across the NB interface in a small time interval dt can be computed by

$$\delta Q = G(T_w - T)A_s dt, \tag{11}$$

where G is the liquid-gas interfacial thermal conductance, T_w is the temperature of the surrounding liquid water which is essentially constant, and A_s is the area of the coalescing NB surface. In Sec. III, we will use MD simulations to calculate G at the nitrogen-water interface of the model NB. The surface area A_s and the volume V of the coalescing NB will also be evaluated from MD simulations. With these known properties, we will predict the variation of gas temperature in the coalescing NB by numerical integration of Eq. (10) and compare the theoretical prediction to that directly obtained from MD simulations.

III. MD SIMULATION OF COALESCENCE OF NBs

A. MD model

The representative MD model system contains two 40-nm N_2 NBs suspended in saturated liquid water at a temperature of 300 K. When close enough, the NBs form a capillary bridge and

coalescence begins as shown in Fig. 1. As the gas bridge forms, liquid is pushed outwards from the center of the simulation box. To accommodate the liquid volume expansion and maintain the liquid pressure at an almost constant value during the coalescence process, two water vapor regions are positioned on both x directions. The periodic boundary conditions (PBCs) are applied in all three directions. The size of the liquid domain is chosen to be large enough so that the characteristics of NB coalescence are almost unaffected by the finite size of the liquid domain.

In all MD simulations, a rigid extended simple point charge (SPC/E) potential model [22] is employed to describe the interactions between water molecules. The Coulombic interactions in the SPC/E potential are evaluated using the Wolf summation [23] with a damping factor of 0.15 Å^{-1} and cutoff distance of 9.0 Å. The Wolf summation technique has been shown to produce reasonable structural results and coexistence densities for SPC/E water [24]. Treating the long-range Coulombic interactions using the Wolf summation allows us to carry out MD simulations in a system containing more than 10 000 000 water molecules for over 7 ns. The LJ potential, with parameters $\sigma = 3.3078$ Å and $\epsilon/k_B = 36.67$ K [25], is used to describe the N-N interactions between the nitrogen molecules whose bond length is fixed at 1.09 Å [26]. The LJ potential is also used to describe the interactions between nitrogen and water molecules with potential parameters determined from the Lorentz-Berthelot mixing rule [27]. The cutoff distance for all LJ interactions is 9.0 Å.

A velocity Verlet algorithm is used to integrate Newton's equations with a time step size of 2 fs. The SHAKE algorithm [28] is used to maintain the rigidity of water and nitrogen molecules in MD simulations. All MD simulations are run using the LAMMPS simulation package [29].

The MD simulation of coalescence of two 40-nm N_2 NBs in the model liquid water includes the following three steps:

Step 1. We begin by inserting 6 132 417 water molecules into the center of a simulation box with a total length of 90 nm in the x direction and a cross section of 65 nm × 48 nm (y and z directions, respectively). The liquid water slab is flanked by two 14-nm vacuum regions in the x direction as shown in Fig. 1, allowing the water molecules to evaporate and form a liquid-vapor interface. The PBCs are applied in all three directions. We carry out an *NVT* simulation to equilibrate the pure water system at a temperature of 300 K using a Nosé-Hoover thermostat [30]. After the system reaches thermal equilibrium, the saturated liquid water coexistent with the saturated vapor water are present in the simulation box.

Step 2. Once the liquid water has reached thermal equilibrium, a spherical region is defined with a diameter of 40 nm. The spherical region is centered in the x and y directions, and the distance between the top z boundary and the top of the sphere is 1.4 nm. Water molecules in the spherical region are replaced with 39 620 N_2 molecules. The number of gas molecules needed for a stable 40-nm NB is calculated using the Laplace pressure and ideal gas relation. After the simulation is equilibrated for 65 ps under *NVT* conditions, all molecules are mirrored in the z direction. This results in two stable N_2 NBs separated by ∼2.8 nm of liquid water. The total number of water and nitrogen molecules in the model system with two N_2 NBs is 10 056 234 and 79 240, respectively.

Step 3. After two N_2 NBs are generated, we turn off the thermostat and carry out an *NVE* simulation. The two NBs are now in Brownian motion. After the *NVE* simulation is carried out for 750 ps, the Brownian motion of the NBs eventually brings them closer together, causing the initial formation of a capillary gas bridge between two NBs. To clearly show the geometry of NBs and the capillary bridge between them, we hide all liquid molecules in the snapshots shown in Fig. 1. In our MD model, a water molecule is defined as a liquid molecule if its potential energy is lower than 0.84 times the average potential energy of a water molecule in the liquid phase. We have successfully used a similar method in our previous work to study the coalescence of nanodroplets and NBs [13,31,32]. Using the potential energy criterion, we can see clear boundaries of NBs as well as the two liquid-vapor water interfaces as shown in Fig. 1. Using snapshots of the system every 5 ps, the bridge radius r_b as a function of time can be directly measured from the projected front view. In addition, the average gas temperature within the coalescing NBs and the average temperature of the surrounding water are output every 2 ps.
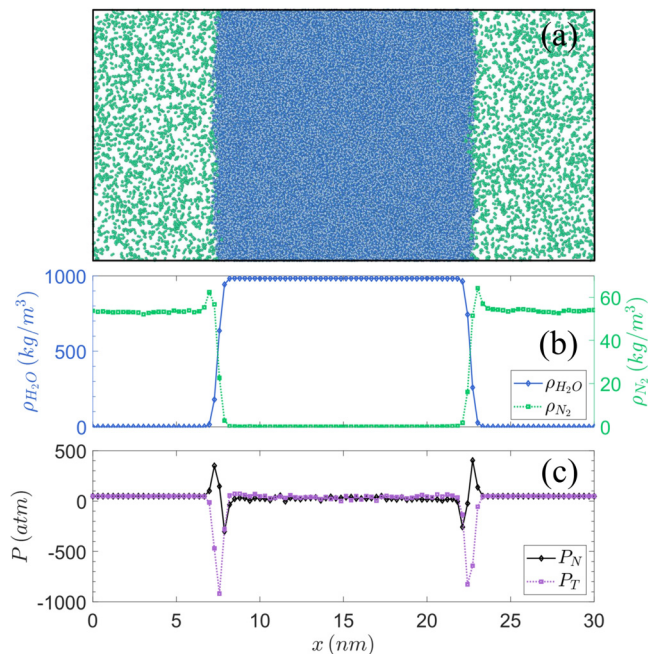
FIG. 2. (a) Snapshot from MD simulation of a liquid water slab coexisting with a nitrogen gas and water vapor mixture. Green, blue, and white dots represent nitrogen, oxygen, and hydrogen atoms, respectively. (b) Density profiles of water (ρ_{H_2O}) and nitrogen (ρ_{N_2}). (c) Pressure profiles in the normal (P_N) and tangential (P_T) directions.

By comparing the measured r_b and T as a function of time from MD simulation with the predictions from the theoretical models described in Sec. II, we will determine if the continuum-based theoretical models give good predictions of the coalescence dynamics and identify the coalescence characteristics of nitrogen NBs in water. To obtain the theoretical predictions, several fluid properties including density, surface tension, viscosity, and liquid-gas interfacial thermal conductance of the model fluid are needed. In Sec. III B, we describe the MD simulations used to determine these properties of the model fluids.

B. Determination of fluid properties

As noted in Sec. III A, the Wolf summation technique significantly enhances the computational efficiency in MD simulations of water systems. However, this technique also leads to a slight underestimate of saturated liquid densities and a lower surface tension of water when compared to those using Ewald sums [24]. Allowing for the very high computational cost in this work, we have to make a compromise to use an MD model which is not exactly the same as the real nitrogen-water system but still reasonably resembles nitrogen NBs in water in experiment. The fluid properties calculated in the following subsections are specifically for the model water whose Coulombic interactions are evaluated using the Wolf summation with the parameters in this work.

1. Determination of density and surface tension

The density ρ and surface tension γ of the model fluid can both be obtained from a single equilibrium MD (EMD) simulation in a system consisting of 110 560 water molecules with two adjacent regions filled with 3900 N_2 molecules as seen in Fig. 2(a). The density of N_2 gas is identical to that in the representative 40-nm NB. The simulation box of the dimensions 30 nm
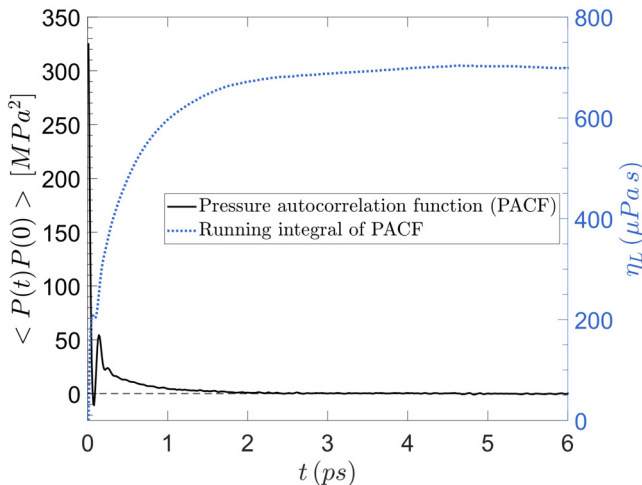
FIG. 3. The pressure-tensor autocorrelation function (PACF) and the running integral of the PACF of the model liquid water at a temperature of 300 K and density of 981 kg/m^3.

$\times$ 15 nm $\times$ 15 nm has PBCs applied in all three directions. The box size is fixed during the EMD simulation. A Nosé-Hoover thermostat is applied to equilibrate the entire system at a temperature of 300 K for 250 ps. After the system reaches equilibrium, a saturated liquid water sandwiched by a gas mixture of N$_2$ and saturated vapor water is present in the simulation box. Subsequently, the thermostat is turned off and an *NVE* simulation is carried out for 500 ps to determine the water density (ρ_{H_2O}), nitrogen density (ρ_{N_2}), and normal (P_N) and tangential (P_T) pressure tensor profiles along the x direction, as shown in Fig. 2. The surface tension is calculated from its mechanical definition [33,34]:

$$\gamma = \frac{1}{2} \int_0^{L_x} [P_N(x) - P_T(x)]dx, \qquad (12)$$

where L_x is the simulation box length in the x direction. From the EMD simulation results at $T = 300$ K, we find the density of saturated liquid water is $\rho = 981 \pm 1$ kg/m^3 and the surface tension of the model water is $\gamma = 0.049 \pm 0.001$ N/m. We carried out similar simulations as described above with different nitrogen densities corresponding to other NB sizes studied in this work and found the density and surface tension of the model water are essentially independent of the nitrogen density in the gas phase. Therefore, we assume the surface tension and water density to be constant for all NB sizes studied in this work.

2. Determination of viscosity

To evaluate the viscosity η_L of the model liquid water at $T = 300$ K and $\rho = 981$ kg/m^3, we carry out a separate EMD simulation in a cubic simulation box containing 4095 model water molecules. The box side length is fixed at 5 nm such that the density of water equals 981 kg/m^3. The PBCs are applied in all three directions. A Nosé-Hoover thermostat is applied for 100 ps to equilibrate the model liquid water to a temperature of 300 K. After the system reaches the thermal equilibrium, we turn off the thermostat, and carry out the simulation in a microcanonical ensemble for 6 ns to calculate the autocorrelation function of the pressure tensor in the model liquid water as shown in Fig. 3. The viscosity is then determined from the Green-Kubo relation [27]:

$$\eta_L = \frac{V}{k_B T} \int_0^\infty dt \langle P_{\alpha\beta}(t)P_{\alpha\beta}(0) \rangle, \qquad (13)$$
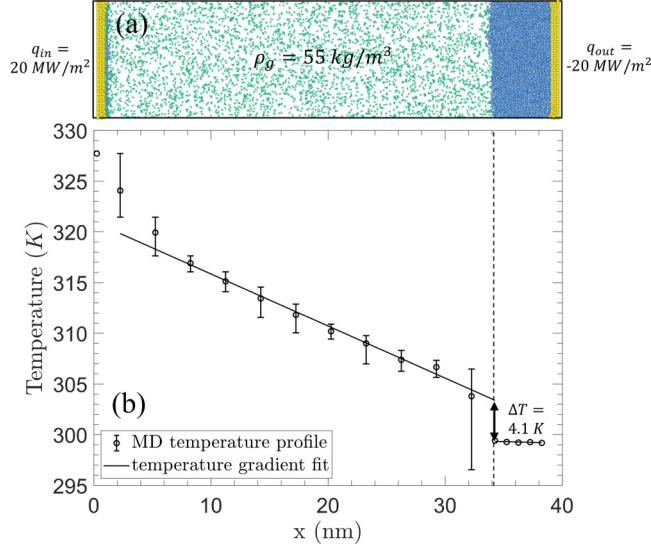
FIG. 4. (a) A snapshot of the NEMD simulation used to obtain the liquid-gas interfacial thermal conductance of the model system. Yellow, green, blue, and white dots represent gold, nitrogen, oxygen, and hydrogen atoms, respectively. (b) Temperature profile at steady state from MD data. The dashed line in (b) indicates the position of the liquid-gas interface.

where

$$P_{\alpha\beta} = \frac{1}{V}\left(\sum_i mv_{i\alpha}v_{i\beta} + \sum_i \sum_{j>i} r_{ij_\alpha}f_{ij_\beta}\right). \tag{14}$$

In Eqs. (13) and (14), V is the system volume, $P_{\alpha\beta}$ is the off-diagonal ($\alpha \neq \beta$) elements of the pressure tensor, t is time, $\langle\cdots\rangle$ means the ensemble average, m is the molecular mass, v_i is the translational velocity of molecule i, and r and f are the intermolecular separation and force, respectively. From the plateau of the running integral [Eq. (13)] shown in Fig. 3, we find $\eta_L = 700 \pm 5\,\mu\text{Pa s}$ which has reasonable agreement with $\eta_L = 729\,\mu\text{Pa s}$ obtained by the SPC/E water models using Ewald sums [35]. Using a similar method, we find the viscosity of the model N_2 gas within the 40-nm NB is $\eta_g = 12.6\,\mu\text{Pa s}$.

3. Determination of liquid-gas interfacial thermal conductance

To evaluate the temperature variation in the coalescing NBs, heat transfer between gas molecules inside the NBs and the surrounding liquid must be considered. Equation (15) shows that the heat transfer rate depends on the interfacial thermal conductance G, which is defined as

$$G = q/\Delta T, \tag{15}$$

where q and ΔT are the heat flux and temperature drop across the liquid-gas interface, respectively. In our previous work, we used nonequilibrium MD (NEMD) simulations and Eq. (15) to evaluate the thermal conductance at liquid-gas interfaces of monatomic fluids and polymers [36,37]. We use a similar method in this work to determine the thermal conductance at the interface between model water and N_2 gas.

As depicted in Fig. 4(a), the model system contains two solid Au plates formed by three fcc atomic layers oriented in the [100] direction with a cross-sectional area of $10 \times 10\,\text{nm}^2$. A liquid water thin film with a 5-nm thickness is positioned on the right Au plate and an adsorbed water

layer is placed on the left Au plate. Nitrogen gas fills the remainder of the simulation box volume at a density equal to that within the representative 40-nm NB. The total box length is 40 nm, and the total number of water and nitrogen molecules is 17 198 and 4138, respectively. PBCs are applied in the y and z directions and the atoms in the outermost Au layers are fixed.

First, a Nosé-Hoover thermostat is applied to the left and right Au plates at 330 and 300 K, respectively. A run time of 6 ns is allowed for the system to reach steady state. Due to the absence of liquid water on the hot plate (except the adsorbed layer which will not evaporate), no evaporation will occur at steady state and heat transfer across the liquid-vapor interface is by conduction only [36,37]. Afterwards, the thermostats are removed and energy is added and subtracted from the hot and cold plates using the eHEX algorithm [38] at a rate of 2 nW, respectively. Thus, a constant heat flux of $q = 20$ MW/m^2 is applied in the NEMD simulation. The simulation is run for 4 ns to ensure steady state is reached at a constant heat flux boundary condition. The average temperature profile shown in Fig. 4(b) is computed using data collected over an additional 4 ns. A temperature gradient fit is calculated using temperature data in the bulk vapor region defined between $x = 6$ nm and $x = 30$ nm. By extrapolating the temperature gradient fit to the liquid-gas interface, the temperature drop is $\Delta T = 4.1 \pm 0.2$ K. Accordingly, we directly obtain $G = 4.9$ MW/m^2 K from Eq. (15).

IV. MODELING RESULTS

A. Representative modeling results

In this section, we present the representative theoretical and molecular modeling results of the coalescence of two 40-nm-diameter N$_2$ NBs in the model liquid water at a temperature of 300 K. Using $R = 20$ nm and the fluid properties obtained in Sec. III B, we calculate the characteristic time $\tau_{\text{inert}} = 0.40$ ns and $\tau_{\text{visc}} = 0.29$ ns for the 40-nm NBs in the model fluid system. Substituting these time constants into Eq. (4), we obtain the theoretical prediction of $r_b(t)$, the scaling exponent in $r_b \propto t^n$, and the ratio of viscous to inertial stresses.

1. Comparison of $r_b(t)$

In Fig. 5(a), we compare the $r_b(t)$ measured directly from the MD simulation to that obtained from Eq. (4), i.e., the governing equation derived from the axisymmetric NS equation. To use Eq. (4) properly in the analysis of NB coalescence, we must check the following three things carefully.

(i) When should we start to use Eq. (4)? As noted in Sec. II A, Eq. (4) is not valid until the NB coalescence exits the ILV regime. To determine at what time we can start to apply Eq. (4) for analysis of the MD data, we estimate the theoretical expansion speed in the ILV regime from Eq. (5) and obtain $dr_b/dt \approx \gamma/\eta_g \approx 3800$ m/s. We fit the MD data of $r_b(t)$ between 10 and 20 ps with a linear function and obtain the bridge expansion speed of $\sim$110 m/s which is significantly lower than the theoretical expansion speed in the ILV regime. Therefore, we believe the NB coalescence has already exited the ILV regime 10 ps after the coalescence begins. Equation (4) should be applicable from $t = 15$ ps. To obtain the theoretical prediction from Eq. (4), we use initial conditions $r_b(t = 15$ ps$) = 1.22$ nm and dr_b/dt $(t = 15$ ps$) = 110$ m/s which are obtained directly from MD simulation results.

(ii) The minimum r_L: r_L is the liquid side principal radius of curvature at the bridge minimum which determines the Laplace pressure, i.e., the driving force for the bridge expansion. In the derivation of Eq. (4), we used the approximation $r_L \approx \Delta z(r_b)$. From the relation $\Delta z(r_b) \approx r_b^2/R$ [see Eq. (2)], one can readily find that $\Delta z(r_b)$ is less than the size of the model water molecule (i.e., $\sigma = 3.17$ Å in the SPC/E potential for water) if r_b is smaller than 2.55 nm. Obviously, the actual r_L should be no smaller than the size of a single water molecule. Otherwise, one would obtain an unrealistically small r_L which results in an unrealistically high Laplace pressure at the early time of the NB coalescence. In our previous study on the coalescence of NBs in a LJ fluid system [13], we showed that using the approximation $r_L \approx \Delta z(r_b)$ at the early time of coalescence results in an overprediction of the expansion speed of the capillary bridge. Therefore, if $r_L = c\Delta z(r_b)$ is less
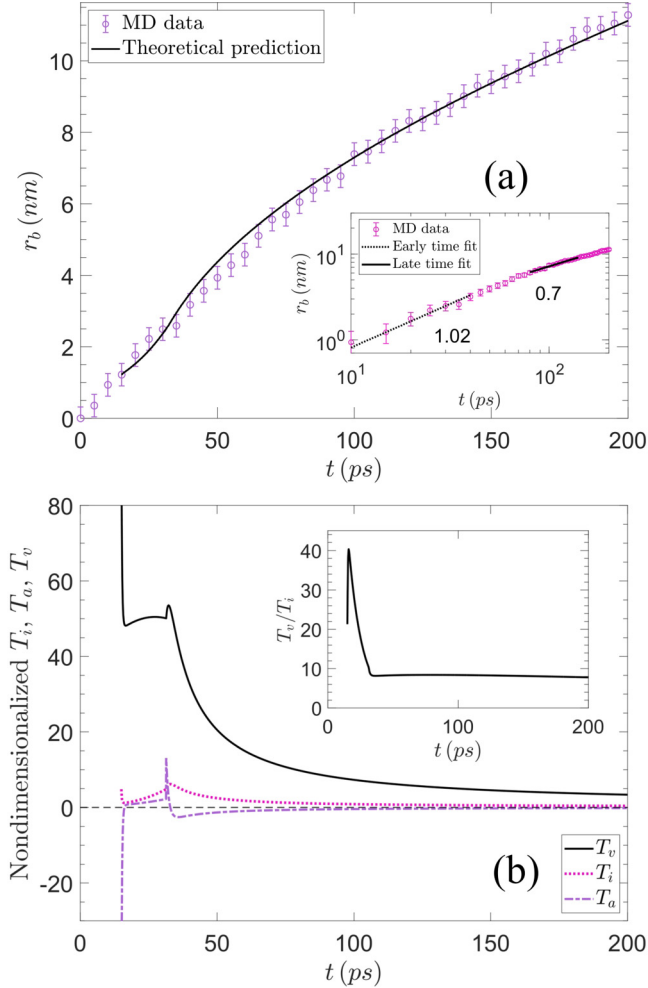
FIG. 5. (a) MD data (measuring snapshots) and theoretical prediction [Eq. (4) with $c = 0.85$] of the minimum bridge radius $r_b(t)$ during the first 200 ps of coalescence of two 40-nm N_2 NBs submerged in the model water (Oh = 0.71). The inset shows the same MD data on logarithmic scale with early and late time slope fits. (b) Viscous, inertial, and acceleration terms in Eq. (4) over time t. The inset shows the ratio of viscous to inertial terms over time t.

than 3.17 Å (i.e., the size of the model water molecule), we will set $r_L = 3.17$ Å in the theoretical model. After implementing the minimum r_L correction, we show in Fig. 5(a) that within 200 ps after the coalescence begins, r_b increases to $\sim$11.2 nm ($r_b/R = 0.56$) and the best fit of the theoretical prediction to the MD data is obtained when the dimensionless constant is $c = 0.85$ in Eq. (4). The optimized c value ($c = 0.85$) indicates $r_L \approx \Delta z(r_b)$ is a reasonable approximation for the liquid side principal radius of the capillary bridge between two NBs.

(iii) The curvature effect on surface tension: At the early time of NB coalescence, the principal radius r_L is comparable to the size of the fluid molecules. The surface tension at these highly curved surfaces could significantly deviate from that at a flat surface [39,40]. The curvature effect on surface tension can be evaluated by the Helfrich expansion [40]

$$\frac{\gamma_c(J, K)}{\gamma} = 1 - \delta J + \frac{k_1}{2\gamma}J^2 + \frac{k_2}{\gamma}K. \tag{16}$$

In Eq. (16), γ_c is the surface tension at a curved surface, γ is the surface tension at a flat interface, $J = 1/r_1 + 1/r_2$ is the total curvature, and $K = (r_1 r_2)^{-1}$ is the Gaussian curvature, where r_1 and r_2 are the principal radii of curvature. At the capillary bridge minimum, $r_1 = -r_b$ and $r_2 = r_L$. In Eq. (16), the three constants δ, k_1, and k_2 are the Tolman length [41], the bending rigidity, and the rigidity constant associated with Gaussian curvature, respectively. To take into account the curvature effect on surface tension of the SPC/E water, we used the Tolman length, bending rigidity, and rigidity constant calculated by Sedlmeier and Netz [42] and by Wilhelmsen *et al.* [43]. In both cases, we found the surface tension only deviates from that of the flat surface by $\sim20\%$ when r_b is less than 2.5 nm and rapidly approaches its flat-surface equivalent once r_b is greater than 4 nm. For r_b in the range of a few nanometers, the minimum r_L correction to the Laplace pressure is more significant than the correction from the curvature effect. As a result, we found the theoretical prediction was nearly unaffected by the curvature effect. Hence, the curvature effect on surface tension is neglected in our theoretical predictions in this work.

2. Comparison of the scaling laws

As shown in the inset of Fig. 5(a), the power function fit ($r_b \propto t^n$) to the MD data exhibits different exponents at the early time and the late time of the coalescence. At early time (10 ps $< t <$ 40 ps) of the coalescence, the scaling exponent from MD simulations is $r_b \propto t^{1.02}$. Although it is close to the scaling law $r_b \propto t$ in the ILV regime, we showed in Sec. IV A that it has already exited the ILV regime since its expansion speed is much lower than that predicted in the ILV regime.

At late times of bubble coalescence, if the coalescence dynamics is in a regime dominated by either liquid viscosity or liquid inertia, the theoretical model predicts the scaling law $r_b \propto t^{0.5}$. Since both the characteristic inertial time τ_{inert} and the characteristic viscous time τ_{visc} in Eqs. (6) and (7) depend on the surface tension, the $r_b \propto t^{0.5}$ scaling law is only valid when the surface tension is a constant. Therefore, we use Eq. (16) with the parameters calculated by Sedlmeier and Netz [42] to estimate the curvature-dependent surface tension at the bridge minimum and select the moment t at which the calculated surface tension deviates less than 1% from that of the flat surface as the starting time for the late time coalescence. Furthermore, from the study of the coalescence dynamics of millibubbles, Thoroddsen *et al.* showed that the scaling law $r_b \propto t^{0.5}$ is valid for $r_b/R < 0.45$ [18]. Hence, we used $r_b/R < 0.45$ as the upper limit of the late time coalescence. The same criteria will also be used to define the late time coalescence of NBs of other sizes in this work. Between the aforementioned upper and lower limits for the late time coalescence, the power function fit to the MD data in Fig. 5(a) shows the exponent $n = 0.7$ which is considerably larger than $n = 0.5$ predicted by the scaling laws for viscous-dominated or inertial-dominated regimes.

The high exponent found in the MD data implies that neither viscous stress nor inertial stress in the surrounding water dominates the coalescence dynamics. To verify this prediction, we calculate the Oh of NBs, which is a good indicator of relative magnitude of viscous and inertial stresses. The recent experimental study on the coalescence of millibubbles shows the crossover from the inertial-dominated regime to the viscous-dominated regime occurs if Oh is close to 0.3 [17]. Using the fluid properties found in Sec. III, we obtain Oh = 0.71 for the model 40-nm N_2 NBs in water. This value is apparently higher than the crossover Oh = 0.3, which indicates that the viscous stress is more significant than the inertial stress in the surrounding liquid during the NB coalescence. To qualitatively determine the ratio of viscous to inertial stresses in the surrounding liquid, we calculate the inertial term T_i, acceleration term T_a, and viscous term T_v in Eq. (4) as a function of time. It is shown in Fig. 5(b) that T_i, T_a, and T_v in Eq. (4) all decay with time after $t > 40$ ps, and the magnitude of T_a is much smaller than T_i and T_v. The inset of Fig. 5(b) shows after $t > 40$ ps the ratio T_v/T_i is nearly a constant around 8. This indicates the magnitude of viscous stress is indeed much greater than that of inertial stress at the later time coalescence. However, it seems the inertial term T_i is still not small enough to be considered negligible since the MD data show the exponent $n = 0.7$ instead of $n = 0.5$.
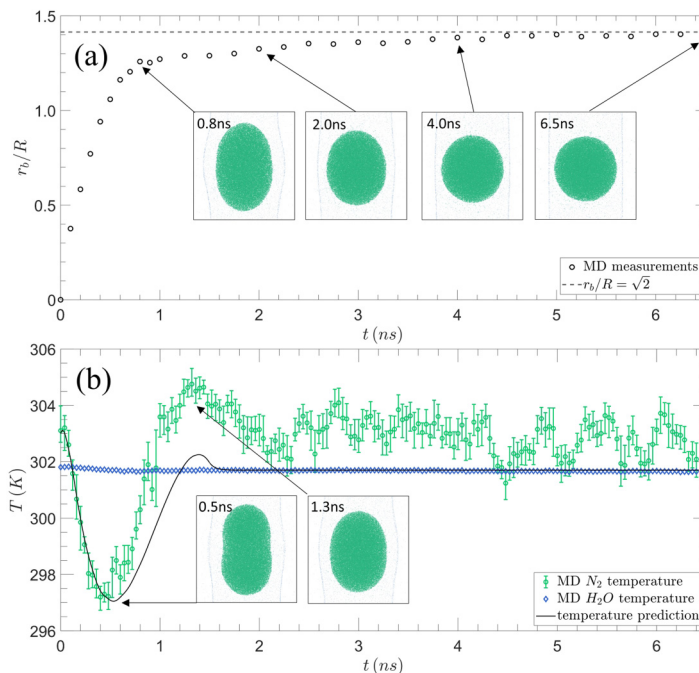
FIG. 6. (a) MD data (measuring snapshots) of the dimensionless bridge radius r_b/R for two 40-nm diameter coalescing N_2 NBs in water. Measurement uncertainties are smaller than the circle symbols showing the MD data. The horizontal dashed line at $r_b/R = \sqrt{2}$ is the theoretical radius of the fully merged NBs. The four insets are snapshots of the model system at 0.8, 2.0, 4.0, and 6.5 ns. (b) Temperature variation of N_2 inside the 40-nm diameter coalescing NBs and H_2O in the surrounding liquid from MD simulations, and the temperature prediction [Eq. (10)] of the gas inside the coalescing NBs. The two insets are snapshots of the model system at 0.5 and 1.3 ns.

To further confirm the high exponent found from the MD simulation of 40-nm NBs in water, we fit the theoretical prediction of $r_b(t)$ at the late time of coalescence with a power function and obtain $r_b \propto t^{0.71}$. The scaling exponents from the theoretical prediction and the MD simulation agree very well. As a comparison, our previous work [13] studied the coalescence of two 40-nm NBs in a LJ fluid system in which Oh $= 0.4$. As the Oh in the LJ fluid system gets closer to the crossover Oh $= 0.3$, it is reasonable to see T_v/T_i in the LJ system is around 4, which is closer to 1 than $T_v/T_i = 8$ in the water system. The power fit to the MD result in the LJ system gives $r_b \propto t^{0.76}$ [13], whose exponent is also apparently greater than $n = 0.5$ in the viscous-dominated regime. In both cases, therefore, the coalescence dynamics at the late time is still in the crossover regime where neither viscous nor inertial stresses in the surrounding liquid dominate. This explains why the growth of the bridge radius does not follow the scaling law $r_b \propto t^{0.5}$ at the late time.

3. Size of fully merged equilibrium NB

To capture the full merge process of the model 40-nm N_2 NBs in water, we carry out the MD simulation for 6.5 ns. The MD results in Fig. 6(a) show the bridge expansion is fast at the initial several hundred picoseconds, but suddenly slows down at $t \approx 800$ ps. The significant change of the expansion speed at $t \approx 800$ ps is mainly caused by the transient convex liquid-vapor interfaces as shown in the inset Fig. 6(a). As the liquid is pushed outwards from the center of the simulation box during NB coalescence, the two originally flat liquid-vapor interfaces become convex surfaces
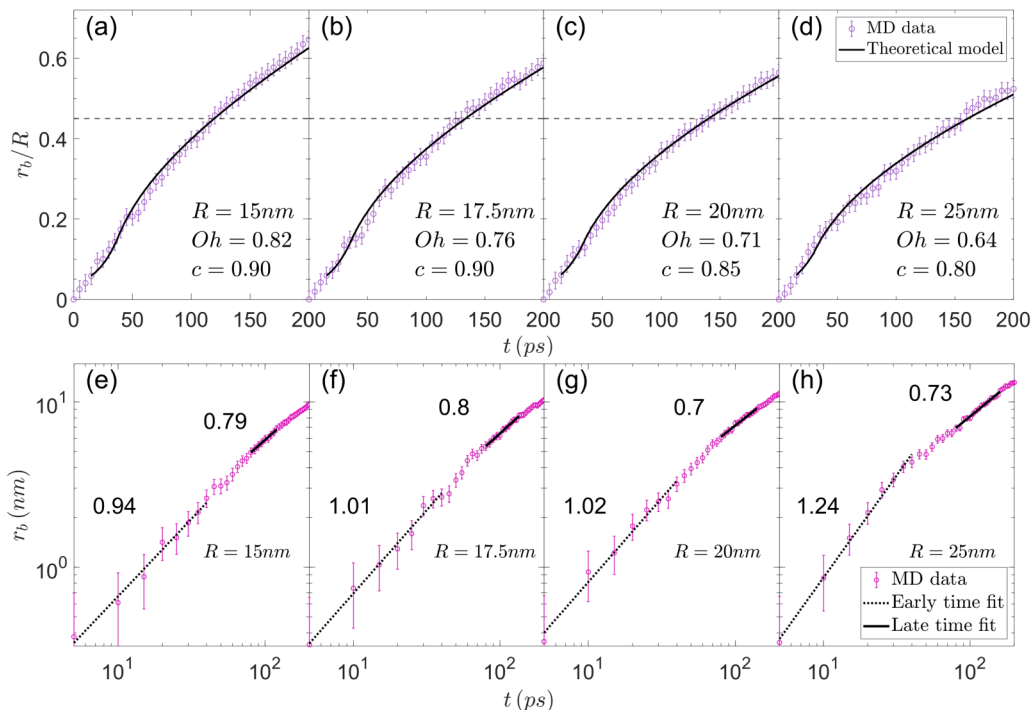
FIG. 7. (a–d) MD data (measuring snapshots) and theoretical prediction [Eq. (4)] of the dimensionless bridge radius r_b/R over time t for 30-, 35-, 40-, and 50-nm diameter NBs. The horizontal dashed line at $r_b/R = 0.45$ marks the upper limit of late coalescence times. The radii, Oh numbers, and c values are shown for all simulation cases. (e–h) MD data and slope fits at early and late coalescence times for the bridge radius $r_b(t)$ on logarithmic scales.

which results in an extra Laplace pressure added to liquid and slows down the bridge expansion. This is an artifact due to the finite size of our model system. In the first 200 ps, however, we show in Fig. 1 that the two liquid-vapor interfaces remain flat. This means our model system is big enough to avoid the finite-size effects on the MD simulation results at the first 200 ps.

At $t \approx 4$ ns, the convex liquid-vapor interfaces return to flat again and remain flat in the rest of the coalescence process as shown in Fig. 6(a). No oscillations of merged NB are found in our MD model which is a result of much higher viscous stress than inertial stress in liquid during NB coalescence. After the two 40-nm NBs fully merge into a bigger NB, it is shown in Fig. 6(a) that the bridge radius approaches $r_b/R = 1.41$, or $\sqrt{2}$, which is consistent with the theoretical prediction in Sec. II C. We ran three additional MD simulations of N_2 NBs in water with diameters of 30, 35, and 50 nm, and find they all follow the $\sqrt{2}$ diameter ratio. In our previous work [13], we also found the fully merged Ne NBs in liquid Ar follows the $\sqrt{2}$ diameter ratio. Hence, our MD simulation results suggest that the $\sqrt{2}$ diameter ratio is one of the coalescence characteristics of bulk NBs.

It is noteworthy that Ma *et al.* recently generated monodispersed NBs of different gases including N_2, O_2, CO_2, etc., in water and measured the size distribution of NBs hours and days after gas injection [19]. In all cases, they found discrete distribution of NB sizes with a uniform increment factor of $\sqrt{2}$. Ma *et al.* infer that the coalescence of two equal-sized bulk NBs in water obeys the $\sqrt{2}$ diameter ratio rule. Our MD simulations provide the direct evidence of the $\sqrt{2}$ diameter ratio for the NB coalescence in water. The $\sqrt{2}$ diameter ratio also indicates that the surface area of a fully merged NB in water is equal to the total surface area of two original NBs.

4. Temperature of N$_2$ gas during coalescence

As the volume and surface area of the coalescing NBs change over time, we expect the temperature and pressure to change accordingly. Figure 6(b) shows the average temperature T of N$_2$ gas inside the coalescing NBs obtained directly from MD simulation. To understand the variation of T of N$_2$ gas from the first law of thermodynamics in Eq. (10), one needs to know how the volume V, surface area A_s, and pressure P of gas inside the coalescing NBs, the interfacial thermal conductance G, and the liquid water temperature T_w change with time t during coalescence.

Among the five parameters (i.e., V, A_s, P, G, and T_w), T_w is essentially a constant around 301.7 K as shown in Fig. 6(b). V and A_s of the coalescing NBs are calculated numerically by reconstructing their shape in computer-aided design (CAD) freeware using the MD snapshots every 50 ps until the coalescing NBs resemble a triaxial ellipsoid at $t = 0.6$ ns. Afterwards, the coalescing NBs are approximated as a triaxial ellipsoid and the diameter in each of the three directions is measured from MD snapshots every 250 ps and used to calculate V and A_s [44]. A fourth order polynomial is fit onto the V and A_s vs t data to use for evaluation. The pressure P inside the coalescing NBs is found from the ideal gas equation with T and V of N$_2$ gas obtained directly from MD simulation. The kinetic theory of gases [45] predicts the thermal conductance G at a liquid-gas interface is proportional to the gas pressure P. Accordingly, we scale the G value obtained in Sec. III B by the transient gas pressure P to predict transient heat transfer rate across the NB surface in Eq. (11). Substituting these known parameters into Eq. (10), we obtain the theoretical prediction of $T(t)$ as shown in Fig. 6(b).

Immediately after coalescence begins, the fast expansion of the gas within the coalescing NBs results in an evident temperature drop inside the NBs. As the gas temperature gets lower than water temperature, the heat transfer from the surrounding liquid to the NBs tends to equilibrate the gas with the liquid. The heat transfer rate increases as gas temperature decreases. At $t \approx 0.5$ ns, the heat transfer rate becomes comparable to the energy loss rate induced by gas expansion, and gas temperature reaches a minimum as shown in Fig. 6(b). The inset of Fig. 6(b) shows the minimum gas temperature occurs when the bridge radius r_b is approximately equal to the NB radius R. In the initial 0.5 ns of the coalescence, the prediction from Eq. (10) agrees with the MD simulation result very well. This implies that the lumped system approximation in our theoretical model for the gas inside the coalescing NBs is reasonable in the initial 0.5 ns of the coalescence.

After $t \approx 0.5$ ns, the gas expansion in the radial direction gradually slows down and at $t \approx 1.0$ ns one starts to see the decrease of the gas volume due to the compression of gas in the longitudinal direction [see the difference between the two snapshots in Fig. 6(b)]. As a result, both the MD data and the theoretical prediction show the temperature inside the NBs increases to a maximum by $t \approx 1.3$ ns and approaches the surrounding liquid temperature for the remainder of coalescence. However, the theoretical prediction from Eq. (10) apparently underestimates the magnitude of gas temperature increase during this time frame. We believe the difference between theoretical and MD results is mainly caused by the lumped system assumption in our theoretical model between $t = 0.5$ ns and $t = 1.5$ ns. In this stage, the gas inside the NBs slowly expands in the radial direction and is rapidly compressed in the longitudinal direction. Hence, the gas flow inside the coalescing NBs is in a nonequilibrium state such that the approximation of the gas as a lumped system with a single temperature and pressure becomes inappropriate. In this case, a more complex theoretical model is required to give a more precise prediction of the gas temperature in the late stage of NB coalescence. Nevertheless, our simple theoretical model, which predicts a reasonable trend of the temperature variation inside the coalescing NBs, implies the gas expansion and the heat transfer between the gas and the surrounding liquid are the two important processes that lead to the variation of gas temperature within the NBs.

B. Effects of NB size on coalescence dynamics

We use methods described in Sec. III A to study coalescence dynamics of three other NB sizes ranging from 30 to 50 nm in diameter. For each NB size, we find $r_b(t)$ directly from the MD
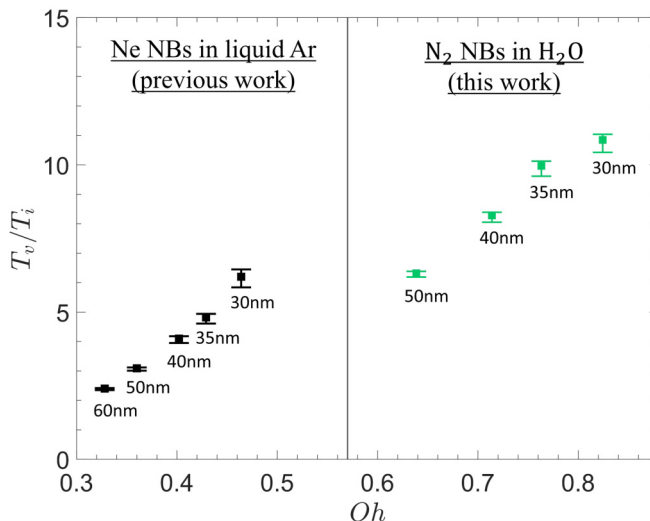
FIG. 8. Ratios of viscous to inertial terms for N_2-H_2O and LJ fluid systems [13]. The error bars show the minimum and maximum ratios calculated during late coalescence times. The number below each symbol shows the NB diameter.

simulation and adjust the value of dimensionless constant c in Eq. (4) to obtain the best fit between the prediction from the continuum-based theoretical model and the MD simulation results. As shown in Figs. 7(a)–7(d), the optimized constants c fall in the range 0.85 ± 0.05, and theoretical predictions have good agreement with MD results for all NB sizes. In our previous study of NB coalescence in a monatomic LJ fluid system [13], we also found the optimized c values are close to 1. This indicates the approximation $r_L(r_b) \approx \Delta z(r_b)$ is reasonable for the principal radius of the capillary bridge between two NBs in both the simple LJ fluid system and the more complex and realistic nitrogen-water system.

As the NB diameter in the model nitrogen-water system decreases from 50 to 30 nm, the corresponding Oh increases from 0.64 to 0.82. A larger Oh implies the viscous stress in the surrounding liquid is more significant on NB coalescence dynamics. To quantitatively define the relative significance of viscous stress to inertial stress in the surrounding liquid, we calculate T_v and T_i from Eq. (4) for each NB size. Similar to the inset of Fig. 5(b), we find the ratio T_v/T_i is nearly a constant during late coalescence times. To show the variation of the ratio T_v/T_i in a wider range of Oh, we combined the calculation results for the nitrogen-water system and those in our previous work for the LJ fluid system [13] in Fig. 8. Although these are results for different fluid systems and at different temperatures, Fig. 8 exhibits the general trend of increasing T_v/T_i with increasing Oh as expected.

As the ratio T_v/T_i increases from 2.4 to 10.9 (see Fig. 8), one would expect the coalescence dynamics to transit from a crossover regime where neither viscous stress nor inertial stress dominates the coalescence dynamics to the viscous-dominated regime, and the scaling exponent in $r_b \propto t^n$ at late times to approach $n = 0.5$. However, the scaling exponents obtained from MD data do not exhibit such a trend. As shown in Figs. 7(e)–7(h), a fit of the MD data for N_2 NBs in water (Oh $= 0.64 - 0.82$) at later times of coalescence gives $r_b(t) \propto t^{0.75 \pm 0.05}$, which is close to $r_b(t) \propto t^{0.76 \pm 0.04}$ for Ne NBs in liquid Ar (Oh $= 0.33 - 0.46$) [13]. In the range of Oh from 0.33 to 0.82, therefore, the MD simulation results show the scaling exponents at the late times of NB coalescence are essentially constant. We attribute the essentially constant scaling exponents in the range of Oh from 0.33 to 0.82 to two main reasons:
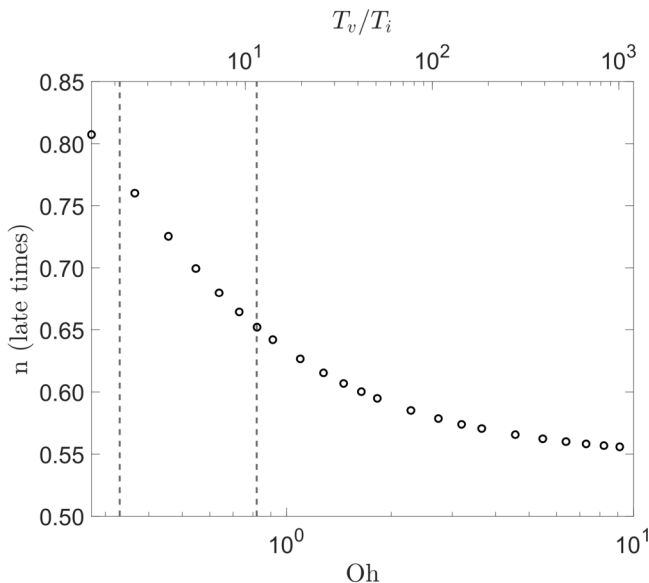
FIG. 9. Theoretical scaling exponents during late coalescence times for 50-nm NBs as the viscosity η_L of water is varied from 0.3 to 10 mPa s in Eq. (4). The dashed lines represent the range of Oh (0.33–0.82) studied.

(i) The range of Oh (0.33–0.82) studied in our MD model is still not wide enough to see a transition into a viscous-dominated regime. Even for the largest ratio $T_v/T_i = 10.9$ at Oh = 0.82, the scaling exponent ($n = 0.79$) at late times is considerably higher than $n = 0.5$ in the viscous-dominated regime, which indicates the inertial term T_i is still non-negligible in this case. To investigate how much we should further increase Oh and T_v/T_i to observe the transition into a viscous-dominated regime, we use Eq. (4) to calculate the scaling exponents at higher Oh and T_v/T_i by artificially increasing the liquid viscosity. All parameters except the liquid viscosity η_L are the same as those in the study of the coalescence of 50-nm diameter N_2 NBs in water. As shown in Fig. 9, the theoretical model predicts the scaling exponent n decreases monotonically with increasing Oh for Oh > 0.3. To see a transition into a viscous-dominated regime, one needs to increase η_L from 0.7 mPa s to at least 7.0 mPa s. For 50-nm N_2 NBs in water, $\eta_L = 7.0$ mPa s corresponds to Oh = 6.4 and $T_v/T_i = 587$. In this case, the scaling exponent decreases to $n \approx 0.56$. Hence, to observe a viscous-dominated regime T_v must be at least hundreds of times greater than T_i.

(ii) If neither viscous stress nor inertial stress dominates the coalescence dynamics, the scaling exponent at late times also depends on the c value in Eq. (4). Note the theoretical prediction in Fig. 9 is obtained when the c value in Eq. (4) is fixed. If the c value for the LJ fluid system (Oh = $0.33 - 0.46$) is the same as that for the water-nitrogen system (Oh = $0.64 - 0.82$), therefore, one would expect higher scaling exponents in the model LJ fluid system. To obtain the best fit to the MD data, however, we find the optimized c values for the LJ fluid system are in the range 1.2 ± 0.2 [13], which is higher than 0.85 ± 0.05 in the water-nitrogen system. A relatively higher c value in Eq. (4) indicates a large radius r_L and smaller Laplace pressure at the capillary bridge which results in slower bridge expansion and lower scaling exponent n. As a result, the relatively higher c value makes the scaling exponent for the LJ fluid system decrease and get close to that for the water-nitrogen system.

From the above analysis we conclude that in the range of Oh studied in our MD model the coalescence dynamics is all in the crossover regime where neither the viscous stress nor the inertial stress in the surrounding liquid dominates the coalescence dynamics.

V. CONCLUSIONS

Using MD simulations coupled with continuum-based theoretical models, we studied the coalescence of bulk N_2 NBs in water with diameters ranging from 30 to 50 nm. The following characteristics of NB coalescence are observed from our modeling results.

(1) At the beginning of coalescence, $r_L(r_b)$, i.e., the principal radius in the liquid side of the capillary bridge between two NBs can be well approximated by $\Delta z(r_b)$, i.e., the gap between two NBs measured in the equivalent configuration before coalescence. To avoid overestimate of the Laplace pressure, i.e., the driving force for the NB coalescence, the principal radius $r_L(r_b)$ should be no smaller than the size of a liquid molecule. In all cases studied, the theoretical prediction of $r_b(t)$ from the axisymmetric NS equation agrees with the MD data very well.

(2) The diameter ratio of a fully merged NB to its daughter NBs is $\sqrt{2}$, which is different from the diameter ratio $\sqrt[3]{2}$ observed in millibubbles and microbubbles. The $\sqrt{2}$ diameter ratio indicates that the surface area of a fully merged NB is equal to the total surface area of two original NBs. The $\sqrt{2}$ diameter ratio also explains the discrete distribution of NB sizes with a uniform increment factor of $\sqrt{2}$ found in recent experiment on characteristics of bulk NBs in water [19].

(3) At the beginning of coalescence, the gas temperature inside the coalescing NBs drops due to the fast expansion of gas. The subsequent heat transfer between surrounding liquid and gas inside NBs and the compression of gas after the bridge radius r_b is greater than the NB radius R increase the gas temperature and eventually equilibrate the gas with the surrounding liquid. The theoretical model based on the first law of thermodynamics gives a reasonable prediction of temperature variation. The difference between the theoretical prediction and the MD simulation results indicates the gas inside the coalescing NBs cannot be approximated as a lumped system once the bridge radius r_b is greater than the NB radius R.

(4) In the range of Oh (0.33–0.82) studied, the viscous stress in the surrounding liquid is a few to ten times greater than the inertial stress and the scaling exponent in $r_b \propto t^n$ at late times of NB coalescence is in the range 0.75 ± 0.05, which is considerably higher than $n = 0.5$ in the viscous-dominated regime or the inertial-dominated regime. To observe a clear transition into the viscous-dominated regime, the theoretical analysis shows the viscous stress in the surrounding liquid must be hundreds of times greater than the inertial stress. Hence, we conclude the coalescence of N_2 NBs in water is in a crossover dynamic regime where neither viscous stress nor inertial stress in the surrounding liquid dominates.

The theoretical models presented in this work are shown to be valid for a nitrogen-water system as well as a LJ monatomic fluid system [13]. Furthermore, Ma *et al.* find the $\sqrt{2}$ diameter ratio rule applies to NBs containing a variety of gases [19]. This evidence suggests universality of coalescence characteristics of NBs in different fluid systems.

[1] M. Alheshibri, J. Qian, M. Jehannin, and V. S. J. Craig, A history of nanobubbles, Langmuir **32**, 11086 (2016).

[2] R. Ahmadi, D. A. Khodadadi, M. Abdollahy, and M. Fan, Nano-microbubble flotation of fine and ultrafine chalcopyrite particles, Int. J. Min. Sci. Technol. **24**, 559 (2014).

[3] J. B. Yianatos, L. G. Bergh, F. Díaz, and J. Rodríguez, Mixing characteristics of industrial flotation equipment, Chem. Eng. Sci. **60**, 2273 (2005).

[4] B. A. Wills and K. Atkinson, The development of minerals engineering in the 20th century, Miner. Eng. 4, 643 (1991).

[5] S. Calgaroto, A. Azevedo, and J. Rubio, Flotation of quartz particles assisted by nanobubbles, Int. J. Miner. Process. 137, 64 (2015).

[6] W. Zhou, H. Chen, L. Ou, and Q. Shi, Aggregation of ultra-fine scheelite particles induced by hydrodynamic cavitation, Int. J. Miner. Process. 157, 236 (2016).

[7] A. Agarwal, W. J. Ng, and Y. Liu, Principle and applications of microbubble and nanobubble technology for water treatment, Chemosphere 84, 1175 (2011).

[8] M. R. Beychok, *Aqueous Wastes from Petroleum and Petrochemical Plants*, 1st ed. (John Wiley & Sons Ltd., New York, 1967).

[9] A. J. Atkinson, O. G. Apul, O. Schneider, S. Garcia-Segura, and P. Westerhoff, Nanobubble technologies offer opportunities to improve water treatment, Acc. Chem. Res. 52, 1196 (2019).

[10] H. Li, L. Hu, D. Song, and F. Lin, Characteristics of micro-nano bubbles and potential application in groundwater bioremediation, Water Environ. Res. 86, 844 (2015).

[11] J. Zhu, H. An, M. Alheshibri, L. Liu, P. M. J. Terpstra, G. Liu, and V. S. J. Craig, Cleaning with bulk nanobubbles, Langmuir 32, 11203 (2016).

[12] Z. H. Wu, H. B. Chen, Y. M. Dong, H. L. Mao, J. L. Sun, S. F. Chen, V. S. J. Craig, and J. Hu, Cleaning using nanobubbles: Defouling by electrochemical generation of bubbles, J. Colloid Interface Sci. 328, 10 (2008).

[13] E. Bird, J. Zhou, and Z. Liang, Coalescence speed of two equal-sized nanobubbles, Phys. Fluids 32, 123304 (2020).

[14] R. L. Stover, C. W. Tobias, and M. M. Denn, Bubble coalescence dynamics, AIChE J. 43, 2385 (1997).

[15] S. Orvalho, M. C. Ruzicka, G. Olivieri, and A. Marzocchella, Bubble coalescence: Effect of bubble approach velocity and liquid viscosity, Chem. Eng. Sci. 134, 205 (2015).

[16] Á. Moreno Soto, T. Maddalena, A. Fraters, D. Van Der Meer, and D. Lohse, Coalescence of diffusively growing gas bubbles, J. Fluid Mech. 846, 143 (2018).

[17] J. D. Paulsen, R. Carmignani, A. Kannan, J. C. Burton, and S. R. Nagel, Coalescence of bubbles and drops in an outer fluid, Nat. Commun. 5, 3182 (2014).

[18] S. T. Thoroddsen, T. G. Etoh, K. Takehara, and N. Ootsuka, On the coalescence speed of bubbles, Phys. Fluids 17, 071703 (2005).

[19] T. Ma, Y. Kimura, H. Yamamoto, X. Feng, A. Hirano-Iwata, and M. Niwano, Characterization of bulk nanobubbles formed by using a porous alumina film with ordered nanopores, J. Phys. Chem. B 124, 5067 (2020).

[20] J. Towns, T. Cockerill, M. Dahan, I. Foster, K. Gaither, A. Grimshaw, V. Hazlewood, S. Lathrop, D. Lifka, G. D. Peterson, R. Roskies, J. R. Scott, and N. Wilkens-Diehr, XSEDE: Accelerating scientific discovery, Comput. Sci. Eng. 16, 62 (2014).

[21] Z. Huang, M. Su, Q. Yang, Z. Li, S. Chen, Y. Li, X. Zhou, F. Li, and Y. Song, A general patterning approach by manipulating the evolution of two-dimensional liquid foams, Nat. Commun. 8, 14110 (2017).

[22] H. J. C. Berendsen, J. R. Grigera, and T. P. Straatsma, The missing term in effective pair potentials, J. Phys. Chem. 91, 6269 (1987).

[23] D. Wolf, P. Keblinski, S. R. Phillpot, and J. Eggebrecht, Exact method for the simulation of Coulombic systems by spherically truncated, pairwise r^{-1} summation, J. Chem. Phys. 110, 8254 (1999).

[24] F. N. Mendoza, J. López-Lemus, G. A. Chapela, and J. Alejandre, The Wolf method applied to the liquid-vapor interface of water, J. Chem. Phys. 129, 024706 (2008).

[25] C. Kriebel, A. Müller, M. Mecke, J. Winkelmann, and J. Fischer, Prediction of thermodynamic properties for fluid nitrogen with molecular dynamics simulations, Int. J. Thermophys. 17, 1349 (1996).

[26] J. Fischer, R. Lustig, H. Breitenfelder-Manske, and W. Lemming, Influence of intermolecular potential parameters on orthobaric properties of fluids consisting of spherical and linear molecules, Mol. Phys. 52, 485 (1984).

[27] R. Scott, M. P. Allen, and D. J. Tildesley, Computer simulation of liquids, Math. Comput. 57, 442 (1991).

[28] J. P. Ryckaert, G. Ciccotti, and H. J. C. Berendsen, Numerical integration of the Cartesian equations of motion of a system with constraints: Molecular dynamics of *n*-alkanes, J. Comput. Phys. **23**, 327 (1977).

[29] S. Plimpton, Fast parallel algorithms for short-range molecular dynamics, J. Comput. Phys. **117**, 1 (1995).

[30] D. J. Evans and B. L. Holian, The Nosé-Hoover thermostat, J. Chem. Phys. **83**, 4069 (1985).

[31] Z. Liang and P. Keblinski, Coalescence-induced jumping of nanoscale droplets on super-hydrophobic surfaces, Appl. Phys. Lett. **107**, 143105 (2015).

[32] R. Bardia, Z. Liang, P. Keblinski, and M. F. Trujillo, Continuum and molecular-dynamics simulation of nanodroplet collisions, Phys. Rev. E **93**, 053104 (2016).

[33] J. G. Kirkwood and F. P. Buff, The statistical mechanical theory of surface tension, J. Chem. Phys. **17**, 338 (1949).

[34] J. P. Walton, D. J. Tildesley, J. S. Rowlinson, and J. R. Henderson, The pressure tensor at the planar surface of a liquid, Mol. Phys. **48**, 1357 (1983).

[35] M. A. González and J. L. F. Abascal, The shear viscosity of rigid water models, J. Chem. Phys. **132**, 096101 (2010).

[36] J. Gonzalez, J. Ortega, and Z. Liang, Prediction of thermal conductance at liquid-gas interfaces using molecular dynamics simulations, Int. J. Heat Mass Transfer **126**, 1183 (2018).

[37] E. Bird, J. Gutierrez Plascencia, and Z. Liang, Thermal transport across the interface between liquid *n*-dodecane and its own vapor: A molecular dynamics study, J. Chem. Phys. **152**, 184701 (2020).

[38] P. Wirnsberger, D. Frenkel, and C. Dellago, An enhanced version of the heat exchange algorithm with excellent energy conservation properties, J. Chem. Phys. **143**, 124104 (2015).

[39] Ø. Wilhelmsen, D. Bedeaux, and D. Reguera, Tolman length and rigidity constants of the Lennard-Jones fluid, J. Chem. Phys. **142**, 064706 (2015).

[40] W. Helfrich, Elastic properties of lipid bilayers: Theory and possible experiments, Z. Naturforsch., C: J. Biosci. **28**, 693 (1973).

[41] R. C. Tolman, The effect of droplet size on surface tension, J. Chem. Phys. **17**, 333 (1949).

[42] F. Sedlmeier and R. R. Netz, The spontaneous curvature of the water-hydrophobe interface, J. Chem. Phys. **137**, 135102 (2012).

[43] Ø. Wilhelmsen, D. Bedeaux, and D. Reguera, Communication: Tolman length and rigidity constants of water and their role in nucleation, J. Chem. Phys. **142**, 171103 (2015).

[44] M. S. Klamkin, Elementary approximations to the area of *n*-dimensional ellipsoids, Am. Math. Mon. **78**, 280 (1971).

[45] F. O. Goodman, *Dynamics of Gas-Surface Scattering* (Academic Press, New York, 1976), pp. 23–31.